Comparison of two force identification methods from full field vibration measurements performed with optical deflectometry

Nicolas Madinier, Alain Berry, Quentin Leclere, Kerem Ege

Comparison of two force identification methods from full field vibration measurements performed with optical deflectometry

N. Madinier [1,2], **A. Berry** [1], **Q. Leclère** [2], **K. Ege** [2]
[1] Université de Sherbrooke, GAUS Departement of Mechanical Engineering,
Sherbrooke, J1K 2R1, QC, Canada
e-mail: **nicolas.madinier@usherbrooke.ca**

[2] Univ Lyon, INSA Lyon, LVA
69621 Villeurbanne, France

Abstract
This paper is concerned with dynamic force identification on thin plates from full field vibration measurements. The main goal of this study is to compare two force identification methods. The first method is the Force Analysis Technique (FAT). It uses a finite difference scheme to discretize the Love-Kirchhoff spatial operator and then resolve the local equation of motion to identify the load. The second method under consideration is the Virtual Fields Method (VFM). In this technique, virtual displacements and curvatures are used to solve the principle of virtual work (PVW). The local aspect and the fact that boundary conditions of the plate need not to be known a priori are important advantages of both methods. In this paper full field vibration measurements are obtained by optical deflectometry. The paper first gives an overview of the Force Analysis Technique, the Virtual Fields Method and the optical deflectometry techniques. It then presents experimental results based on deflectometry measurements.

1 Introduction

In the past, several methods have been developed to identify the dynamic loads applied on a structure from the measured vibration response. Two methods are addressed in this paper: the Force Analysis Technique and the Virtual Field Method. The Force Analysis Technique (FAT) was first developed by Guyader and Pézerat to identify the pressure field applied on a beam [1], a plate or a shell. This method is based on the strong form of the local equilibrium. Since then, FAT has been the subject of several developments like the Corrected Force Analysis Technique (CFAT) which allows identifying the pressure field at higher frequencies. This method has been formulated for isotropic plates [2] and recently to more complex structures such as laminated plates [3]. FAT and CFAT have also been used to identify structural parameters (Young's moduli, damping factor) of isotropic plates [4, 5] and orthotropic plates [6, 7].

The second method addressed in this paper is the Virtual Field Method (VFM). This method is based on the principle of virtual work (PVW), a weak form of the equation of equilibrium. The VFM consists in solving the PVW using a carefully selected set of virtual displacements, called virtual fields [8]. The key point of the method is the choice of those virtual fields. Contrary to FAT, VFM was first developed to identify mechanical constitutive parameters. Since then the method has been applied to identify stationary dynamic loadings on bending plates [9, 10]. This identification has also been developed to identify non-stationary excitations (such as diffuse acoustic fields and turbulent flows) thanks to a time resolved identification [11, 12].

In this study, full-field vibration measurements performed by a fast camera and optical deflectometry on an isotropic thin plate are used as inputs of the force identification methods. Optical deflectometry provides local bending slopes with a large time and space resolution. Optical deflectometry has been already coupled

with VFM in the work of O'Donoughue et al. ([11, 12] but to the best of the authors' knowledge the use of optical deflectometry measurements in force identification with FAT has never been reported.

This paper first details the basic principles of FAT and VFM and then provides details on the optical full-field measurements and processing. Finally, experimental results of force identification on an isotropic plate are presented.

2 Identification methods

2.1 Force analysis technique

FAT is based on a strong form of the local equilibrium. We consider a homogeneous isotropic Love-Kirchhoff plate of thickness h. This plate is submitted to a harmonic transverse loading $q(\mathbf{x},t) = \tilde{q}(\mathbf{x})e^{j\omega t}$ [Pa] where $\mathbf{x}$ is the position of an arbitrary point of the plate and j= $\sqrt{-1}$. The out-of-plane displacement is denoted by $w(\mathbf{x},t) = \tilde{w}(\mathbf{x})e^{j\omega t}$ [m]. The local equilibrium equation of the plate is [2] :

$$\tilde{q}(\mathbf{x}) = -\rho h\tilde{w}(\mathbf{x})\omega^2 + D\left(\frac{\partial^4\tilde{w}(\mathbf{x})}{\partial x^4} + 2\frac{\partial^4\tilde{w}(\mathbf{x})}{\partial x^2\partial y^2} + \frac{\partial^4\tilde{w}(\mathbf{x})}{\partial y^4}\right) \tag{1}$$

where ρ is the mass density of the plate, $D = \frac{Eh^3}{12(1-\nu^2)}$ is the flexural stiffness and x, y are the cartesian coordinates on the plate.

In FAT, the 4-th order derivatives in Eq. (1) are estimated by finite differences [2]:

$$\begin{aligned}
\frac{\partial^4\tilde{w}}{\partial x^4} &\simeq \delta_\Delta^{4x} = \frac{1}{\Delta^4}\sum_{r=-2}^{2}\Gamma_r\tilde{w}(x+r\Delta,y)\\
\frac{\partial^4\tilde{w}}{\partial y^4} &\simeq \delta_\Delta^{4y} = \frac{1}{\Delta^4}\sum_{r=-2}^{2}\Gamma_r\tilde{w}(x,y+r\Delta)\\
\frac{\partial^4\tilde{w}}{\partial^2 x\partial^2 y} &\simeq \delta_\Delta^{2x2y} = \frac{1}{\Delta^4}\sum_{p=-1}^{1}\sum_{q=-1}^{1}\Psi_{pq}\tilde{w}(x+p\Delta,y+q\Delta)
\end{aligned} \tag{2}$$

where Δ is the spacing between two consecutive points in the experimental mesh and $\Gamma_{-2} = \Gamma_2 = 1, \Gamma_{-1} = \Gamma_1 = -4, \Gamma_0 = 6$, $\Psi_{00} = 4$, $\Psi_{-10} = \Psi_{10} = \Psi_{0-1} = \Psi_{01} = -2$ and $\Psi_{-1-1} = \Psi_{11} = \Psi_{1-1} = \Psi_{-11} = 1$. The external pressure estimate by FAT is given by [2]:

$$\tilde{q}^{\text{FAT}}(\mathbf{x}) = -\rho h\tilde{w}(\mathbf{x})\omega^2 + D(\delta_\Delta^{4x} + \delta_\Delta^{4y} + \delta_\Delta^{2x2y}) \tag{3}$$

Therefore, to estimate the applied pressure at point $\mathbf{x}$, the measurement of 13 displacements around x is needed.

One of the strengths of FAT is its local aspect. Indeed, the boundary conditions of the structure or the vibration response outside those 13 points are not required to estimate the load at $\mathbf{x}$. On the other hand, FAT is sensitive to measurement noise. The 4$^{\text{th}}$ order derivatives, amplify measurement noise and the results of the method will no longer be reliable in low frequency. In response to this issue, a low-pass filtering in the wavenumber domain is applied at each frequency. This operation avoids noise amplification in the high wavenumber domain. In this study, the low-pass wavenumber filter is applied when extracting data from the deflectometry measurements (see section 3.2). The low-pass filtering is related to the number of measurement points by flexural wavelength λ:

$$n = \frac{\lambda}{\Delta} = \frac{2\pi}{k\Delta} \tag{4}$$

where $k = \sqrt[4]{\frac{\rho h}{D}}\sqrt{\omega}$ is the flexural wavenumber of the plate. When the number of measurement points by wavelength is large, the method will have a greater sensibility to measurement noise.

2.2 Virtual Fields Method

2.2.1 Principe of Virtual Work

The starting point of the Virtual Field Method (VFM) is the Principle of Virtual Work (PVW), which is a weak form of the equation of equilibrium. This principle is given again for a Love-Kirchhoff plate of surface S submitted to a harmonic transverse loading [9]:

$$\frac{h^3}{12}\int_S \boldsymbol{\mathcal{K}}^{v^T}(\mathbf{x})\mathbf{Q}(\mathbf{x})\tilde{\boldsymbol{\mathcal{K}}}(\mathbf{x})\mathrm{dS} - h\omega^2\int_S \rho\tilde{w}(\mathbf{x})w^v(\mathbf{x})\mathrm{dS} = \int_S \tilde{q}^{\mathrm{VFM}}(\mathbf{x})w^v(\mathbf{x})\mathrm{dS} \tag{5}$$

where

- $\tilde{\boldsymbol{\mathcal{K}}}(\mathbf{x})$ denotes the bending curvatures of the plate at position $\mathbf{x}$. They are given by:

$$\tilde{\boldsymbol{\mathcal{K}}}(\mathbf{x}) = \begin{pmatrix}\mathcal{K}_{xx}\\ \mathcal{K}_{yy}\\ \mathcal{K}_{xy}\end{pmatrix} = -\begin{pmatrix}\partial^2/\partial x^2\\ \partial^2/\partial y^2\\ \partial^2/\partial x\partial y\end{pmatrix}\tilde{w}(\mathbf{x}) \tag{6}$$

- $\mathbf{Q}(\mathbf{x})$ is the 3x3 elastic matrix of the plate, here considered constant over S and given by:

$$\mathbf{Q}(\mathbf{x}) = \frac{E}{1-\nu^2}\begin{pmatrix}1 & \nu & 0\\ \nu & 1 & 0\\ 0 & 0 & \frac{1-\nu^2}{2(1+\nu)}\end{pmatrix} \tag{7}$$

- $w^v(\mathbf{x})$ and $\boldsymbol{\mathcal{K}}^v(\mathbf{x})$ are respectively the virtual displacement and associated virtual curvatures (in Eq. (5) the superscript ^{T} denotes the transpose matrix).

2.2.2 Virtual fields

The virtual fields $w^v(\mathbf{x})$ and $\mathcal{K}^v(\mathbf{x})$ are the key quantities of the VFM. The PWV is resolved with any virtual displacement w^v C^1 (continuity of the virtual displacement and its first derivatives). Also, in order to avoid additional unknown forces and moments at the plate's edges in the PWV, the virtual fields need to be kinematically admissible (KA). For example, if the plate is simply-supported along all edges, to be KA, the virtual displacement should also be null at the edges.

Since any C^1 KA function over S can be a virtual displacement, a choice needs to be made. In our case, piecewise virtual displacements are used. These displacements are defined over a virtual mesh like in the Finite Element Method but they are limited to a small sub-domain of S [8]. One advantage of piecewise virtual displacements compared to virtual displacements defined over the whole surface S is their flexibility. In our case we consider a virtual displacement based on the Hermite16 interpolation functions used in the Finite Element Method. This field fulfills the C^1 continuity condition [8]. The virtual displacements are defined over a rectangular virtual window S_v (scanning the plate surface) composed of 4 quadrants. In order to eliminate the virtual work of transverse forces and bending moments, at the boundary of S_v the virtual displacement and its normal derivatives are equal to zero on the edges of S_v. Each quadrant posseses 4 nodes for a total of 9 degrees of freedom. For each position of the window over the plate surface, these nodes correspond to points of the experimental mesh. The virtual window, virtual displacements and virtual

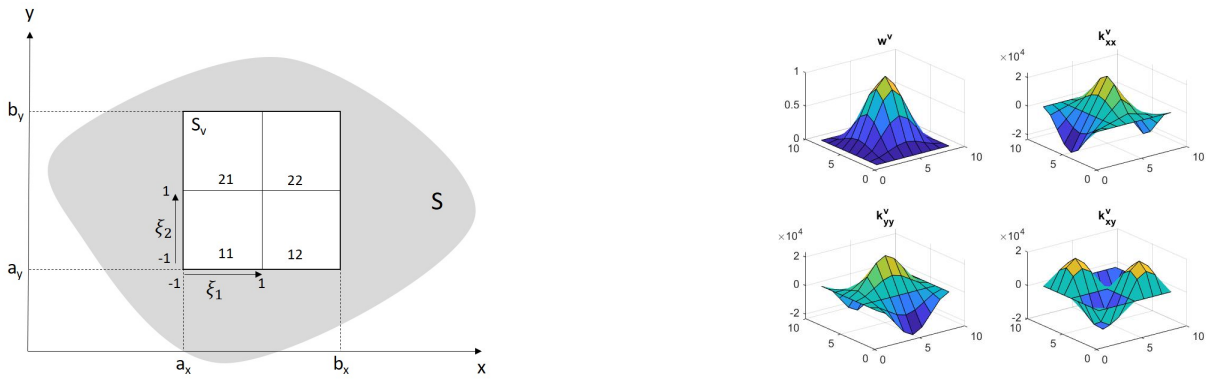

(a) (b)

Figure 1: (a) Virtual window S_v defined on the plate surface S (b) Virtual displacement w^v and curvatures $\mathcal{K}^v_{xx}$, $\mathcal{K}^v_{yy}$, $\mathcal{K}^v_{xy}$ over the virtual window

curvatures are shown in Figure 1. The virtual displacement over each quadrant is defined by [9]:

$$\begin{aligned} w^v(x,y) &= H_2^0(\xi_1)H_2^0(\xi_2) \text{ on quadrant 11} \\ w^v(x,y) &= H_1^0(\xi_1)H_2^0(\xi_2) \text{ on quadrant 12} \\ w^v(x,y) &= H_2^0(\xi_1)H_1^0(\xi_2) \text{ on quadrant 21} \\ w^v(x,y) &= H_1^0(\xi_1)H_1^0(\xi_2) \text{ on quadrant 22} \end{aligned} \tag{8}$$

where ξ_1 and ξ_2 are non-dimensional coordinates defined for each quadrant, $H_1^0(\xi) = \frac{1}{4}(2+\xi)(1-\xi)^2$ and $H_2^0(\xi) = \frac{1}{4}(2+\xi)(1+\xi)^2$. The curvatures related to these displacements are detailed in appendix A. Each virtual window will be moved over S and for each position Eq. (5) is solved over S_v. The loading is searched as a concentrated force $\tilde{f}^{\text{VFM}}(\omega)$ applied at the center point $\mathbf{x_c}$ of each virtual window. Since $w^v = 1$ at the center of the window the right term of Eq. (5) becomes :

$$\int_{S_v} \tilde{q}^{\text{VFM}}(\mathbf{x}) w(\mathbf{x})^v \text{dS} = \int_{S_v} \tilde{f}^{\text{VFM}}(\omega)\delta(\mathbf{x}-\mathbf{x_c}) w(\mathbf{x})^v \text{dS} = \tilde{f}^{\text{VFM}}(\omega) \tag{9}$$

The force estimated by VFM in the center of the window is then given by:

$$\tilde{f}^{\text{VFM}}(\omega) = \frac{h^3}{12}\int_{S_v} \boldsymbol{\mathcal{K}}^{v^T}(\mathbf{x})\mathbf{Q}(\mathbf{x})\tilde{\boldsymbol{\mathcal{K}}}(\mathbf{x})\text{dS} - h\omega^2 \int_{S_v} \rho\tilde{w}(\mathbf{x}) w^v(\mathbf{x})\text{dS} \tag{10}$$

The integrals on the right-hand side of Eq. (10) are approximated by sums over the points of the measurement grid. Note that in comparison to the local equilibrium Eq. (1), the PVW in Eq. (10) requires only second-order spatial derivatives of the transverse displacement to obtain the loading (instead of 4th-order derivatives in Eq. (1)), making the approach a priori less sensitive to measurement noise.

3 Deflectometry measurements

3.1 Basic principles

Optical deflectometry is a full-field non-invasive technique which measures the local slopes of the transverse displacement fields of flat structures. A schematic of a deflectometry setup is shown in figure 2. The surface of the plate must have a mirror-like finish. On this surface the specular reflection of the grid, placed in front of the plate at a distance L, is observed. A high-speed camera records this specular reflection, as shown by the example at the bottom of figure 2. When a dynamic load is applied on the plate, the transverse deformation

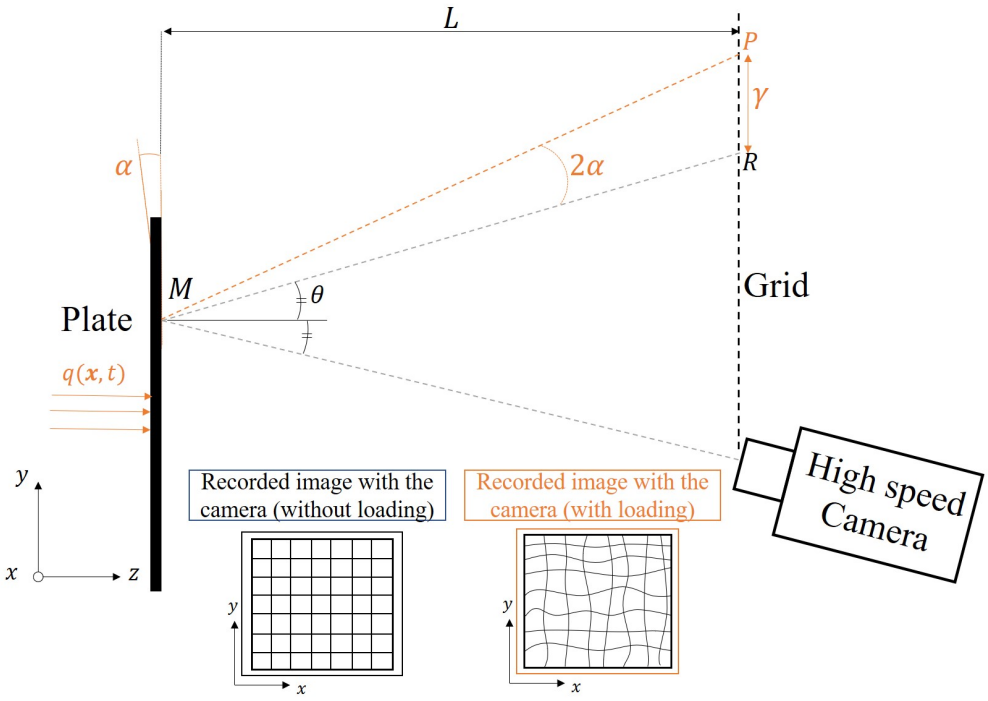

Figure 2: Schematic of a optical deflectometry set-up

of the plate creates a time-varying distortion of the grid reflection as shown in right bottom of figure 2. The deflectometry measurement consists in recording these distortions with the high-speed camera. The bending vibration of the plate leads to a local slope α at point M, which is now the reflection of point P of the grid instead of R. The shift $\overline{PR}$ is noted γ. With the small angle approximation for θ and α [11], γ is given by:

$$\gamma = 2L\alpha \tag{11}$$

Another expression of γ can be obtained with the local phase variations in the grid images. The phase map of a reference image recorded in the absence of load is compared to the phase map of a distorted image. The phase maps are extracted with a Windowed Discrete Fourier Transform (WDFT) algorithm that performs a 2D discrete Fourier transform of the distorted grid image. The phase of the first Fourier component of the grid images is then obtained with a spatial phase shifting and windowing with a kernel triangular window. Since the phase values returned are between $[-\pi, \pi]$, an unwrapping algorithm is applied. The difference $\Delta\phi(x, y) = \phi_d(x, y) - \phi_r(x, y)$ is kept, with $\phi_d(x, y)$ and $\phi_r(x, y)$ the phases extracted from the distorted and reference images respectively. The shift γ can then be locally obtained with the relation [11]:

$$\gamma = \frac{p}{2\pi}\Delta\phi \tag{12}$$

where p is the grid pitch [m], i.e. the spatial period of the grid. The corresponding pitch on the plate is $p/2$ because of the reflection. In practice, two phase maps are obtained: one according to local x-slopes, $\Delta\phi_x(x, y)$ and one according to local y-slopes, $\Delta\phi_y(x, y)$. Combining Eqs. 11 and 12, the local slopes according to x and y are given by:

$$\begin{cases} \alpha_x &= \frac{p}{4\pi L}\Delta\phi_x(x, y) \\ \alpha_y &= \frac{p}{4\pi L}\Delta\phi_y(x, y) \end{cases} \tag{13}$$

3.2 Extraction of plate displacements from deflectometry measurements

An important setting of the measurement setup is that the number N of pixels in the camera sensor corresponding to a grid pitch on the image must be an integer. Consequently, for each grid period, a measurement

point will be obtained. This number N cannot be too small to have a good estimation of the local phase shift or too high in order to avoid a sub-optimal use of the camera by having few measurement points [12]. This calibration is mandatory for the use of the WDFT algorithm and allows reducing Moiré interference. A good calibration over the whole image is very hard to achieve in practice. However, the kernel triangular window used in the WDFT algorithm helps reducing the error due to miscalibration [11]. In addition to the WDFT and 2D unwrapping algorithms, the data are spatially smoothed with a second kernel triangular window of size $N \times N$. The pressure $\tilde{q}^{\text{FAT}}$ is obtained via Eq. (1) and the finite difference scheme Eq. (2) to estimate 4th-order spatial derivatives of displacements. On the other hand, for VFM, the PVW in Eq. (5) requires both the displacement and curvature fields of the structure. In practice, the curvature fields are obtained by calculating the numerical gradient of the slope fields. An interesting point is that VFM requires only one spatial integration and one spatial derivation to be applied to slope fields. The integration of the slopes to obtain out-of-plane displacement field is a more complex operation that is performed here in the wavenumber domain. Here, $\hat{\alpha_x}(k_x, k_y)$, $\hat{\alpha_y}(k_x, k_y)$ and $\hat{w}(k_x, k_y)$ denote the 2D spatial Fourier transforms of α_x and α_y and w. For k_x and k_y non-zero, $\hat{w}(k_x, k_y)$ is given by :

$$\begin{cases} \hat{w}(k_x, k_y) &= \frac{\hat{\alpha_x}(k_x,k_y)}{jk_x} \\ \hat{w}(k_x, k_y) &= \frac{\hat{\alpha_y}(k_x,k_y)}{jk_y} \end{cases} \tag{14}$$

This system is solved using the least square approach:

$$\hat{w}(k_x, k_y) = -\frac{jk_x\hat{\alpha_x}(k_x, k_y) + jk_y\hat{\alpha_y}(k_x, k_y)}{k_x^2 + k_y^2} \tag{15}$$

The $k_x = 0$, $k_y = 0$ singularity is solved by first assuming that $\hat{w}(0, 0) = 0$ (the spatial DC component of the displacement field is 0). The out-of-plane displacement is recovered by an inverse 2D Fourier transform of Eq.(14). The DC value of the displacement is then modified by imposing the boundary condition of the plate. In the experimental work (see the next section), the plate is simply-supported along its four edges. A zero-displacement at the center point of the left edge is imposed on the displacement field.

4 Experimental results

4.1 Experimental set-up

A 0.42×0.48 m^2 rectangular aluminum panel, of thickness 3.2 mm ($\rho = 2700$ kg/m^3, $\nu = 0.3$ $E = 70$ GPa) is mounted on a metallic frame with simply-support boundary conditions. The camera set-up calibration is made with $N = 7$ pixels per grid pitch. The deflectometry setup is shown in figure 3a. The distance between the grid and the panel is $L = 1.51$ m and the grid pitch is $p = 8$ mm in each direction, thus the spatial resolution of the structural vibration is $p/2 = 4$ mm. The smallest calculated flexural wavelength in the frequency range [180 ; 5660] Hz is 73.7 mm. The experimental mesh is composed of 116×101 points. The images are recorded with a Photron SA-X2 high-speed camera. The maximum resolution of the camera is 1024×1024 pixel. The recording is made with a frame rate of 12,000 fps and a recording time of 1.49 s. The plate is excited by a shaker (Bruël & Kjaer 4810) with a broadband input filtered over octave bands. Five measurements, one for each of the five octave band considered, are made. The bands considered are 250, 500, 1000, 2000 and 4000 Hz. The shaker injects forces in the plate via a small metallic circular tablet of diameter 13 mm which is glued to the plate at position $x = 0.055$ m, $y = 0.16$ m relative to the bottom left corner of the plate. A force sensor (PCB 208C03) is mounted on the shaker to measure the injected force.

4.2 Force identification results

Once the slope fields have been extracted, a 2D spatial Fourier transform is performed on these fields at each time step so that Eq (15) can be applied. A 2D inverse Fourier transform of the results of Eq (15) is realized to obtain the displacement field over time. The numerical differentiation of the slope fields to obtain the

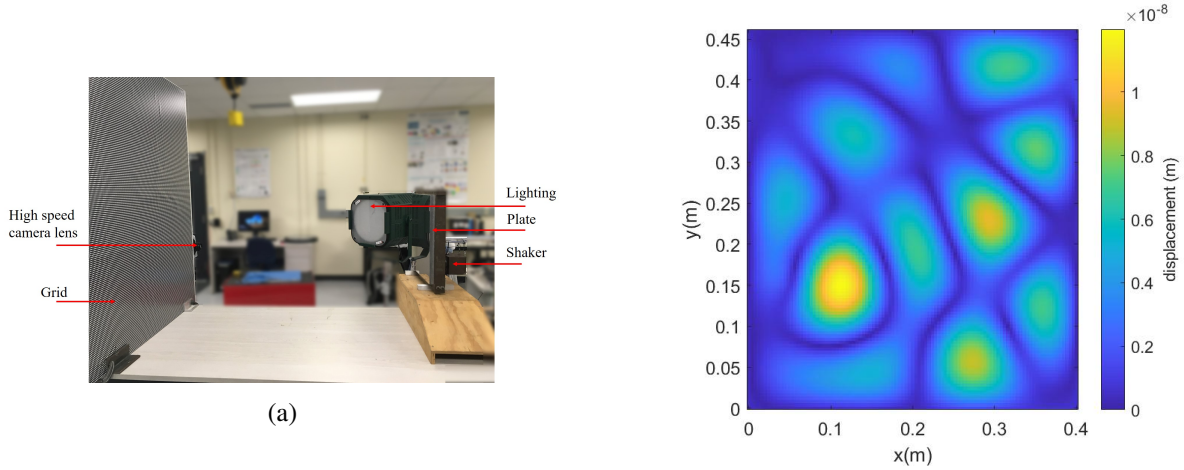

(a) (b)

Figure 3: (a) Experimental set-up (b) Out-of-plane displacement at 1 kHz

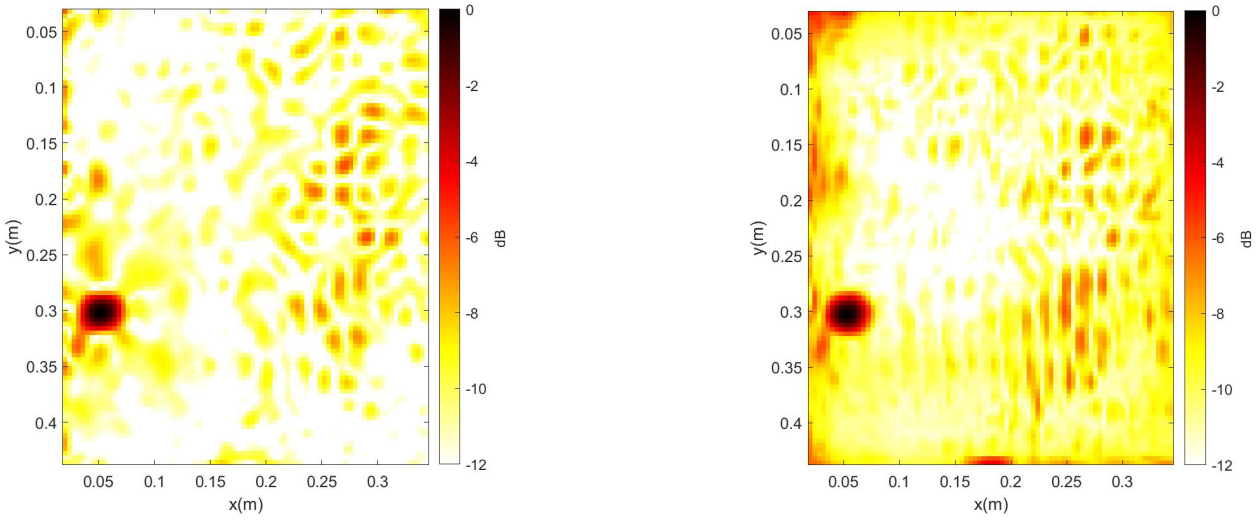

(a) (b)

Figure 4: Identified force with (a) VFM and(b) FAT integrated between 180 and 5660 Hz (in dB normalized by the maximum value for each map, over a 12dB range)

curvature fields is directly performed in the time domain. A time Fourier transform of the displacement and curvature is then performed to obtain the displacement at each point in the frequency domain. The 4th order derivatives of the displacements are calculated using the displacement field in the frequency domain. VFM and FAT are finally applied in the frequency domain. An example of the out-of-plane displacement at 1 kHz is shown in figure 3b. In order to reduce the noise sensitivity of FAT in the estimation of 4th order spatial derivatives of plate displacements, the number of points n per flexural wavelength (Eq. (4)) is reduced by taking the step Δ in the finite difference scheme equal to twice that in the experimental mesh. The window in the VFM has a size of 9×9 pixels. At each frequency a complex cartography of the identified forces is obtained for both methods. The moduli of these maps are integrated between 180 and 5660 Hz. The result is shown in figure 4. In addition to these results, in figure 5 are shown the maps of the identified loads averaged over 250, 500, 2000 and 4000 Hz octave band. The force applied on the plate is well localized with both methods. By comparing figure 5b, and 5h it can be highlighted that FAT's maps are less noisy when the frequency increases (i.e. when the parameter n decreases).

Since a force sensor has been mounted on the shaker, the force magnitudes obtained with the sensor and the methods can be compared to FAT and VFM predictions. Since FAT identifies a pressure, a spatial integration

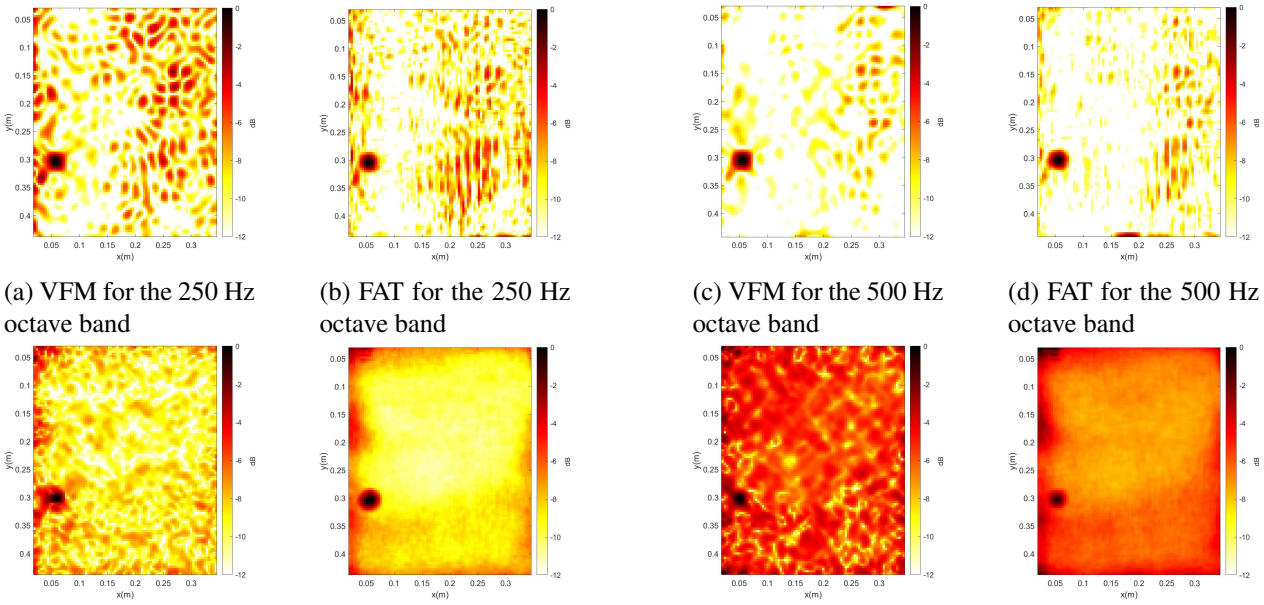

(a) VFM for the 250 Hz octave band

(b) FAT for the 250 Hz octave band

(c) VFM for the 500 Hz octave band

(d) FAT for the 500 Hz octave band

(e) VFM for the 2000 Hz octave band

(f) FAT for the 2000 Hz octave band

(g) VFM for the 4000 Hz octave band

(h) FAT for the 4000 Hz octave band

Figure 5: Identified force with FAT and VFM integrated over 250, 500, 2000 and 4000 Hz octave bands (in dB normalized by the maximum value for each map, over a 12dB range))

of the pressure is necessary in order to recover the force magnitude. The area considered here corresponds to the surface of the tablet mounted at the end of the shaker. The force identified with VFM is averaged on the same surface. The comparison of these results over all octave bands is shown in figure 6. On figure 7 the same results are integrated over each third octave band between 200 and 5000 Hz. The force magnitude predicted with FAT and VFM is satisfactory even though some divergence with the results from the direct measurement are observable. In low frequency FAT slightly overestimates the force magnitude due to measurement noise. Above 4 kHz, the actual force injected by the shaker decreases significantly and FAT and VFM predictions become also contaminated by measurement noise.

5 Conclusion

In this study the Virtual Fields Method (VFM) and the Force Analysis Technique (FAT) were used to identify the load applied on a simply supported thin aluminum plate. The measurements were performed by optical deflectometry. The applied force can be well located and quantified on the five octave bands considered in these experiments (from 250 Hz to 4 kHz). The simplicity of FAT and its local aspect are its main advantages. However, its sensitivity to noise can be a problem if no regularization is applied to remove high wavenumber components. Here no extra low-pass wavenumber filter has been applied as the procedure used to extract the vibratory field already involves a low-pass wavenumber filter.

The Virtual Fields Method, requires less regularization than FAT, however the choice of the virtual fields is crucial in this approach. This aspect of VFM means that it may be more complex to apply compared to FAT.

In the continuity of this study, the comparison of both methods could be realized in the future on the identification of the material parameters of complex panels. The calculation of the Love-Kirchhoff spatial operator directly with the slope fields is a subject that may also be studied in the future.

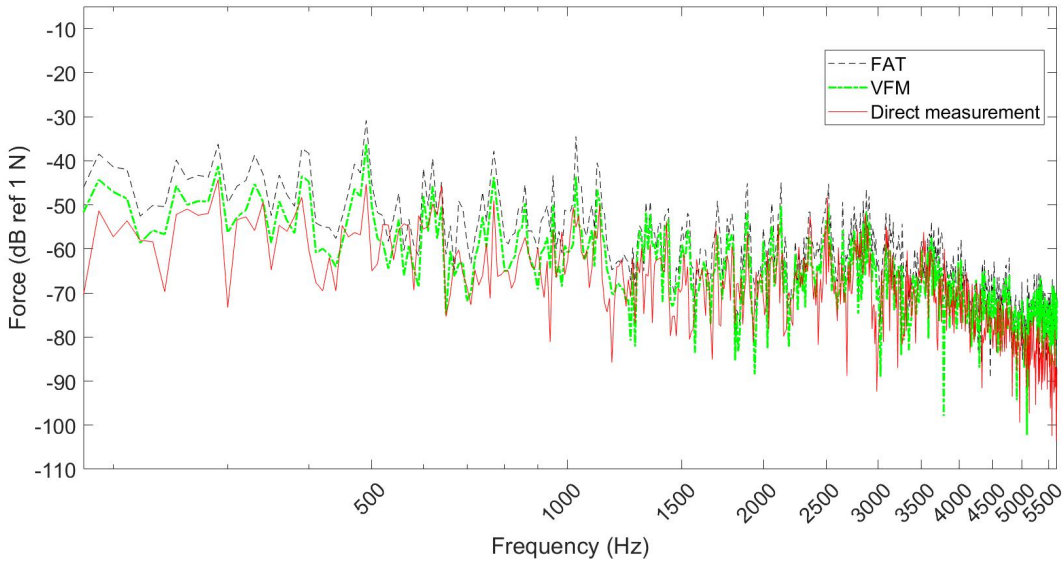

Figure 6: Force spectra (in dB ref 1 N) identified with FAT (thin black dashed line) VFM (thick green dash-dotted line) and direct measurement (thin continuous red line)

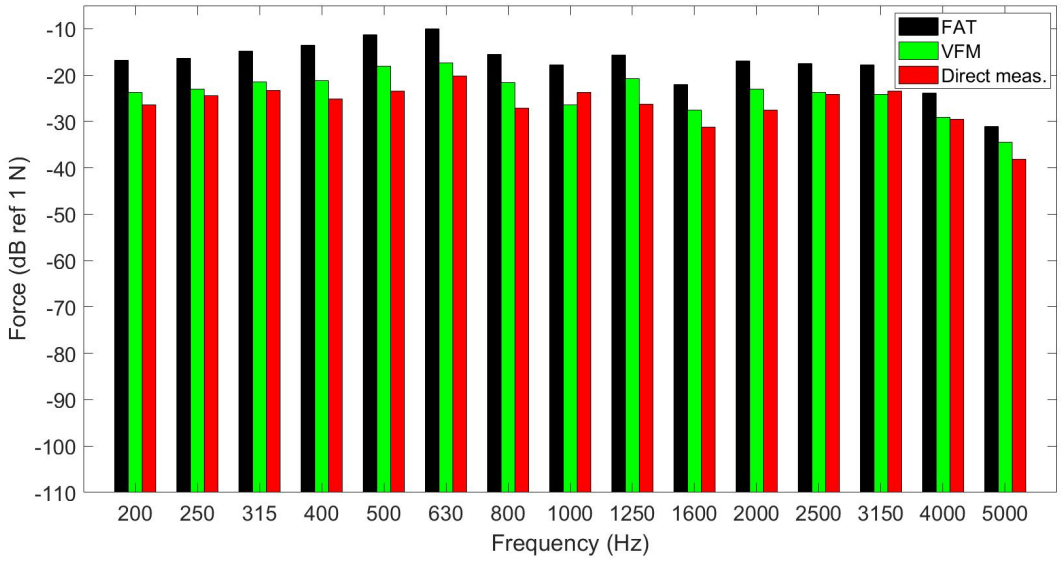

Figure 7: Force spectra (in dB ref 1 N) identified with FAT (black line) VFM (green) and direct measurement (red) integrated over each each third octave band between 200 and 5000 Hz

Acknowledgements

The authors would like to thank Dr. Patrick O'Donoughue from Le Mans Université, France for his essential participation in the measurements and his useful advices concerning the post-processing of the deflectometry images.

References

[1] C. Pezerat and J.-L. Guyader, "Two inverse methods for localization of external sources exciting a beam," *Acta Acustica*, vol. 3, pp. 1–10, 1995.

[2] Q. Leclère and C. Pézerat, "Vibration source identification using corrected finite difference schemes," *Journal of Sound and Vibration*, vol. 331, no. 6, pp. 1366–1377, Mar. 2012, number: 6. [Online]. Available: https://linkinghub.elsevier.com/retrieve/pii/S0022460X11008807

[3] F. Marchetti, K. Ege, and Q. Leclère, "Development of the Corrected Force Analysis Technique for laminated composite panels," *Journal of Sound and Vibration*, vol. 490, p. 115692, Jan. 2021. [Online]. Available: https://linkinghub.elsevier.com/retrieve/pii/S0022460X20305228

[4] F. Ablitzer, C. Pézerat, J.-M. Génevaux, and J. Bégué, "Identification of stiffness and damping properties of plates by using the local equation of motion," *Journal of Sound and Vibration*, vol. 333, no. 9, pp. 2454–2468, Apr. 2014. [Online]. Available: https://linkinghub.elsevier.com/retrieve/pii/S0022460X13010535

[5] Q. Leclère, F. Ablitzer, and C. Pézerat, "Practical implementation of the corrected force analysis technique to identify the structural parameter and load distributions," Sep. 2015. [Online]. Available: https://linkinghub.elsevier.com/retrieve/pii/S0022460X15003570

[6] F. Ablitzer, C. Pézerat, B. Lascoup, and J. Brocail, "Identification of the flexural stiffness parameters of an orthotropic plate from the local dynamic equilibrium without a priori knowledge of the principal directions," *Journal of Sound and Vibration*, vol. 404, pp. 31–46, Sep. 2017. [Online]. Available: https://linkinghub.elsevier.com/retrieve/pii/S0022460X1730425X

[7] F. Marchetti, "Modélisation et caractérisation large bande de plaques multicouches anisotropes," Ph.D. dissertation, Institut National des Sciences Appliquées de Lyon, Lyon, France, Dec. 2019. [Online]. Available: https://tel.archives-ouvertes.fr/tel-02443702/document

[8] F. Pierron and M. Grédiac, *The Virtual Fields Method: Extracting Constitutive Mechanical Parameters from Full-field Deformation Measurements*. New York: Springer-Verlag, 2012. [Online]. Available: https://www.springer.com/gp/book/9781461418238

[9] A. Berry, O. Robin, and F. Pierron, "Identification of dynamic loading on a bending plate using the Virtual Fields Method," *Journal of Sound and Vibration*, vol. 333, no. 26, pp. 7151–7164, Dec. 2014, number: 26. [Online]. Available: https://linkinghub.elsevier.com/retrieve/pii/S0022460X1400710X

[10] A. Berry and O. Robin, "Identification of spatially correlated excitations on a bending plate using the Virtual Fields Method," *Journal of Sound and Vibration*, vol. 375, pp. 76–91, Aug. 2016. [Online]. Available: https://linkinghub.elsevier.com/retrieve/pii/S0022460X16300177

[11] P. O'Donoughue, O. Robin, and A. Berry, "Time-resolved identification of mechanical loadings on plates using the virtual fields method and deflectometry measurements," *Strain*, vol. 54, no. 3, p. e12258, Jun. 2018, number: 3. [Online]. Available: https://onlinelibrary.wiley.com/doi/10.1111/str.12258

[12] P. O'Donoughue, O. Robin, and A. Berry, "Time-space identification of mechanical impacts and distributed random excitations on plates and membranes," *Proceedings of the Institution of Mechanical Engineers, Part C: Journal of Mechanical Engineering Science*, vol. 233, no. 18, pp. 6436–6447, Sep. 2019, number: 18 Publisher: IMECHE. [Online]. Available: https://doi.org/10.1177/0954406219839094

Appendix

A Expression of the virtual curvatures

The virtual curvatures are given by [9] :

$$\begin{aligned}
\frac{\partial^2 w^v(x,y)}{\partial x^2} &= \frac{16}{(b_x-a_x)^2} H_2^{0"}(\xi_1) H_2^0(\xi_2) \text{ on quadrant 11} \\
\frac{\partial^2 w^v(x,y)}{\partial x^2} &= \frac{16}{(b_x-a_x)^2} H_1^{0"}(\xi_1) H_2^0(\xi_2) \text{ on quadrant 12} \\
\frac{\partial^2 w^v(x,y)}{\partial x^2} &= \frac{16}{(b_x-a_x)^2} H_2^{0"}(\xi_1) H_1^0(\xi_2) \text{ on quadrant 21} \\
\frac{\partial^2 w^v(x,y)}{\partial x^2} &= \frac{16}{(b_x-a_x)^2} H_1^{0"}(\xi_1) H_1^0(\xi_2) \text{ on quadrant 22}
\end{aligned} \tag{16}$$

Where $H_1^{0"} = \frac{3}{2}\xi$ and $H_2^{0"} = -\frac{3}{2}\xi$

$$\begin{aligned}
\frac{\partial^2 w^v(x,y)}{\partial y^2} &= \frac{16}{(b_y-a_y)^2} H_2^0(\xi_1) H_2^{0"}(\xi_2) \text{ on quadrant 11} \\
\frac{\partial^2 w^v(x,y)}{\partial y^2} &= \frac{16}{(b_y-a_y)^2} H_1^0(\xi_1) H_2^{0"}(\xi_2) \text{ on quadrant 12} \\
\frac{\partial^2 w^v(x,y)}{\partial y^2} &= \frac{16}{(b_y-a_y)^2} H_2^0(\xi_1) H_1^{0"}(\xi_2) \text{ on quadrant 21} \\
\frac{\partial^2 w^v(x,y)}{\partial y^2} &= \frac{16}{(b_y-a_y)^2} H_1^0(\xi_1) H_1^{0"}(\xi_2) \text{ on quadrant 22}
\end{aligned} \tag{17}$$

$$\begin{aligned}
\frac{\partial^2 w^v(x,y)}{\partial x \partial y} &= \frac{16}{(b_x-a_x)(b_y-a_y)} H_2^{0'}(\xi_1) H_2^{0'}(\xi_2) \text{ on quadrant 11} \\
\frac{\partial^2 w^v(x,y)}{\partial x \partial y} &= \frac{16}{(b_x-a_x)(b_y-a_y)} H_1^{0'}(\xi_1) H_2^{0'}(\xi_2) \text{ on quadrant 12} \\
\frac{\partial^2 w^v(x,y)}{\partial x \partial y} &= \frac{16}{(b_x-a_x)(b_y-a_y)} H_2^{0'}(\xi_1) H_1^{0'}(\xi_2) \text{ on quadrant 21} \\
\frac{\partial^2 w^v(x,y)}{\partial x \partial y} &= \frac{16}{(b_x-a_x)(b_y-a_y)} H_1^{0'}(\xi_1) H_1^{0'}(\xi_2) \text{ on quadrant 22}
\end{aligned} \tag{18}$$

with $H_1^{0'} = \frac{3}{4}(\xi^2-1)$ and $H_2^{0"} = -\frac{3}{4}(\xi^2-1)$